DNA methylation protects cancer cells against non-canonical senescence

Xiaoying Chen[1,*], Kosuke Yamaguchi[1,7,*,#], Brianna Rodgers[1], Delphine Goerhig[2], David Vindrieux[2], Xavier Lahaye[3], Matthieu Nolot[1], Laure Ferry[1], Pierre Dubus[4], Fumihito Miura[5], Takashi Ito[6], Nicolas Manel[3], David Bernard[2], Pierre-Antoine Defossez[1,#]

1: Université Paris Cité, CNRS, Epigenetics and Cell Fate, F-75013 Paris, France.
* contributed equally
# Authors for correspondence: yamako0801@icloud.com, pierre-antoine.defossez@cnrs.fr

2: Equipe Labellisee La Ligue Contre Le Cancer, Centre de Recherche en Cancerologie de Lyon, Inserm U1052, CNRS UMR 5286, Centre Leon Berard, Universite de Lyon, Lyon, France

3: Institut Curie, PSL Research University, INSERM, U932, Paris, France.

4: Department of Histology and Pathology, Centre Hospitalier Universitaire de Bordeaux, 33000, Bordeaux, France.
BRIC U1312, INSERM, Bordeaux Institute of Oncology, Université de Bordeaux, 33000, Bordeaux, France.

5: Life Science Data Research Center, Graduate School of Frontier Sciences, the University of Tokyo
Kashiwanoha 5-1-5, Kashiwa, Chiba 277-8561, Japan

6: Department of Biochemistry, Kyushu University Graduate School of Medical Sciences, Fukuoka, Fukuoka, 812-8582, Japan.

7: Department of Chromosome Science, National Institute of Genetics, Research Organization of Information and Systems (ROIS), Yata 1111, Mishima, Shizuoka, 411-8540, Japan.

Abstract

Aberrant DNA methylation patterns are a hallmark of human cancers, prompting targeting of DNA methylation machinery to be explored as an anti-tumor strategy. DNA methyltransferase 1 (DNMT1) and ubiquitin like With PHD and Ring finger domains 1 (UHRF1) are crucial enzymes for DNA methylation maintenance. Unlike DNMT1, UHRF1 is overexpressed in most cancers and is a proven oncogene in vivo. Our previous work revealed that the degree of DNA methylation loss induced by UHRF1 depletion is more severe than DNMT1 depletion in colorectal cancer cells, indicating that targeting UHRF1 may be a more effective approach. Using an advanced chemical/genetic system, the auxin-inducible degron (AID) technology, we monitored the long-term effects of removing UHRF1 and/or DNMT1 in cancer cells, deciphering the mechanistic basis through bioinformatic tools. We found that chronic DNA demethylation triggers cancer cells to undergo cellular senescence. The loss of UHRF1 results in a more rapid and profound senescence phenotype than DNMT1 loss. Intriguingly, this senescence is not accompanied by DNA damage and functions independently of canonical senescence pathways such as p53 and p16/pRB. Non-canonical pathway investigations revealed that cytosolic p21 accumulation contributes to antiapoptosis during senescence. The suppression of cyclic GMP-AMP synthase (cGAS) also alleviates the senescence-associated secretory phenotype (SASP) and lysosomal activity, and this process is independent of stimulator of interferon genes (STING). Finally, xenograft experiments verified our findings in vivo. Our results highlight how DNA methylation protects cancer cells from non-canonical senescence and demonstrate the potential of targeting UHRF1 as a novel avenue for anticancer treatments.

INTRODUCTION

DNA methylation is a chemical modification which must be maintained during DNA replication in mammals. This process occurs through DNA methyltransferases (DNMTs) that transfer a methyl group (CH_3) from S-adenyl methionine (SAM) to the fifth carbon of a cytosine residue to generate 5-methylcytosine (5mC), predominantly in the context of CpG dinucleotides (1). DNA methylation has several vital biological functions including transcriptional regulation, control of transposable elements, X-chromosome inactivation, and genomic imprinting (2–5).

Abnormal DNA methylation is a hallmark of tumorigenesis and cancer development. This disrupted DNA methylation pattern is characterized by global hypomethylation, which commonly occurs in regions of repeated elements, and focal hypermethylation at tumor suppressor gene (TSG) promoter regions. Given its reversible nature, targeting the DNA methylation machinery offers promising therapeutic strategies for cancer treatment (6).

DNA methylation patterns are established by the de novo DNA methyltransferase 3 alpha (DNMT3A) and DNA methyltransferase 3 beta (DNMT3B), and are maintained throughout DNA replication by DNA methyltransferase 1 (DNMT1). This DNA methylation maintenance also requires the partnership of the regulator enzyme ubiquitin like with PHD and RING finger domains 1 (UHRF1), which recognizes hemi-methylated CpG sites, subsequently recruiting and activating DNMT1 to maintain DNA methylation during cell division (3, 7, 8). Our previous research demonstrated that UHRF1 also interacts with both DNMT3A and DNMT3B, inhibiting ten-eleven translocation methylcytosine dioxygenase 2 (TET2) - mediated active DNA demethylation (9). Interestingly, unlike DNMT1, UHRF1 is an oncogene found to be overexpressed in a majority of cancers; this overexpression causes cancer in animal models, and its continued expression is required for the growth and survival of tumor cells (10, 11). Depleting UHRF1 leads to global DNA hypomethylation in cancer cells (9, 11). Moreover, the degree of DNA demethylation induced by UHRF1 depletion is higher than DNMT1 depletion in HCT116 (9), indicating that targeting UHRF1 may be a more effective strategy than targeting DNMT1. However, it is still not clear that if the cancer cells suffer more at the cellular level in the absence of UHRF1 than in the absence of DNMT1.

The cellular response to DNA methylation loss varies by the cell type, sources and degree of stresses. In some cancer cells, DNA hypomethylation achieved by using DNA demethylating agent (5-azacytidine/Vidaza and 5-aza-deoxycytidine/Decitabine) can induce either apoptosis (12–14) or senescence (13, 15, 16). These drugs act through crosslinking DNMTs to DNA, which subsequently induces DNA damage and causes cytotoxicity. Therefore, it is difficult to separate the effects of DNA methylation loss from those of DNA damage. There are currently no commercial inhibitors effectively targeting UHRF1, highlighting the importance of using genetic tools that can better identify the cellular and dynamic consequences of UHRF1 or DNMT1 loss.

Because UHRF1 is essential for cancer cell survival, obtaining homozygous UHRF1 knockout lines was not possible; we therefore employed the auxin-inducible degron (AID) system in colorectal cancer cell lines (9). In this system, the degron-fused protein can be recognized by an E3 ligase upon the addition of a small molecule, auxin, followed by ubiquitination and a total, rapid proteasomal degradation of the target (17, 18). Through this

system the primary defect of the protein depletion can be observed. Our previous work has demonstrated that UHRF1 and/or DNMT1 depletion inhibits cancer cell proliferation through processes independent of apoptosis, however the underlying mechanism and cellular phenotype have not been elucidated.

Here we present data showing that cancer cells with chronic DNA demethylation undergo cellular senescence. The loss of UHRF1 results in a more rapid and profound senescence phenotype that DNMT1 loss. This senescence is not accompanied by DNA damage and is independent of canonical senescence pathways such as p53 and p16/RB. Our research further explores non-canonical factors involved in the induction and maintenance of this senescence phenotype, deepening the potential clinical implications for targeting DNA methylation in cancer cells.

Materials and Methods

In vitro experiments

Cell lines and cell culture

The HCT116 cells are male. Their derivative expressing OsTIR1 under a doxycyclin-inducible promoter was developed and published by the Kanemaki lab (17), and we described in a previous publication how we used them to generate UHRF1-mAID, DNMT1-mAID, and UHRF1-mAID/DNMT1-mAID degron cells using the original AID (AID1) system. We also used DLD1 cells (male) constitutively expressing the OsTIR1(F74G) improved variant (PMID: 33177522) to generate degron alleles of UHRF1-mAID2 and DNMT1-mAID2, in a second version (AID2) system (18).

For the current publication, we generated a new series of degron lines, in the HCT116 AID2 background. Following our previously published protocol (9), cells were transfected with CRISPR-Cas9 and donor plasmids using Lipofectamine 2000. After 700 µg/mL G418 or 100 µg/mL hygromycin selection, we obtained HCT116 AID2 lines (UHRF1-mAID2, DNMT1-mAID2 and UHRF1-mAID2/DNMT1-mAID2). Other human cancer cell lines including HT29 (female), A549 (male), and HeLa (female) were acquired from the ATCC.

To achieve degradation of the AID-tagged protein, AID1 cells were seeded and incubated with 2 µg/mL doxycycline (Dox) and 20 µM auxinole for 24hr. Afterwards, the medium was replaced with a fresh medium containing 2 µg/mL Dox and 500µM indole-3-acetic acid (IAA, auxin). For AID2 cells, they were seeded one day prior to the addition of medium containing 1 µM 5-Ph-IAA, an IAA derivative. The medium with either Dox/auxin or 5-Ph-IAA was replaced every two days.

HCT116 and HT29 cells were cultured in McCoy's 5A medium supplemented with 10% FBS, 2 mM L-glutamine, 100 U/mL penicillin and 100 µg/mL streptomycin. DLD1 cells were cultured in RPMI-1640 medium with the same supplements as above. A549 and HeLa cells were cultured in DMEM medium also supplemented identically. All cultures were incubated at 37°C under a humidified atmosphere containing 5% CO_2. Cells were tested monthly for mycoplasma infection. The cell identity was confirmed by short tandem repeat (STR) analysis.

Plasmid construction

shRNA targeting Scramble (negative control), cGAS or p21 were cloned into the pLKO.1-blast vector (Addgene #26655). Plasmids were generated using PCR, restriction enzymes, or Gibson Assembly (NEB) Cloning techniques. The vector pLenti X2 Blast/shp16 (w112-1) (Plasmid #22261) and pLenti X2 Blast/pTER shLUC (w618-1) (Plasmid #20962) were from Addgene. Human papillomavirus type 16 (HPV16) E6-E7 combined genes were amplified from the template vectors (pLXSN E6-E7, Addgene #52394) and then cloned into pLenti6.2/V5-DEST lentiviral vector (Invitrogen). gRNA targeting STING and control are gifts from Nicolas Manel (Institute Curie, FR). All plasmids underwent sequencing prior to their utilization.

Cell counting

Cells were initially seeded at 0.125 million per well in 6-well plates and cultured in medium supplemented with 2 µg/mL doxycycline (Dox) and 20 µM auxinole. On the following day (Day 0), the medium was refreshed with one containing 2 µg/mL Dox and 500µM auxin. Cell counts

were performed on Day 4, after which cells were passaged at a density of 0.25 million, and again on Day 8. The Dox/auxin-containing medium was renewed every two days. A BioRad automated cell counter was employed to determine total cell numbers.

Protein extraction

Cells were harvested after trypsinization, washed twice with PBS, and lysed with RIPA buffer (Sigma-Aldrich) with protease inhibitor cocktail (Roche) and phosphatase inhibitor cocktail 3 (Sigma-Aldrich) for 20 min on ice, and then sonicated with series of 30 s ON / 30 s OFF for 5 min on a Bioruptor device (Diagenode) and centrifuged at 16,000 g for 15 min at 4 °C. The supernatant was collected and quantified by Pierce BCA protein assay kit (Thermo Fisher Scientific).

Cell fractionation

Cells pellets (5 million) were gently lysed in 500 µL of hypotonic buffer (20 mM of Tris-HCl (pH 7.6), 3 mM of $MgCl_2$, 10 mM of NaCl) supplemented with protease inhibitor cocktail (Roche) and phosphatase inhibitor cocktail 3 (Sigma-Aldrich). Incubate on ice for 20 min. Add 25 µL detergent (10% NP-40) and vortex for 10 seconds at highest setting. Following centrifugation for 10 min at 3,000 rpm at 4 °C, the supernatants were collected as the cytoplasmic fraction. Pellets were washed twice with hypotonic buffer and then were lysed by 200 µL RIPA buffer. After incubation on ice for 30 min, the lysates were centrifuged for 30 min at 13,000 rpm at 4 °C. The supernatants then were collected as the nuclear fraction.

Western blot

Equivalent amounts of protein extract per sample were mixed with NuPage 4X LDS Sample Buffer and 10X Sample Reducing Agent (Thermo Fisher Scientific) and denatured at 95°C for 5 min. Samples were resolved on a pre-cast SDS-PAGE 4-12% gradient gel (Invitrogen) and transferred to a nitrocellulose membrane (Millipore). The membranes were blocked in 5% (w/v) non-fat milk in PBST buffer (PBS with 0.1% Tween 20) or 5% (w/v) bovine serum albumin in TBST buffer (TBS with 0.1% Tween 20), then incubated overnight at 4°C with the appropriate primary antibodies diluted in 5% milk PBST or 5% BSA TBST. All the antibodies are listed in Supplementary Table 1.

BrdU labeling and FACS

To analyze the cell cycle, HCT116 cells were seeded in a 6 well plate and treated with Dox/auxin for up to 8 days. The cells collected at Day 0, Day4 and Day8 were treated with a BrdU (Sigma-Aldrich) pulse 1 hour before collection. For collection, cells were washed, trypsinized and resuspended in PBS. Afterwards, ice-cold absolute ethanol was added dropwise to each sample for fixation. Once each time point was collected and fixed, samples were denaturated in 2 N HCl for 15 minutes at room temperature, followed by two washes in 1% BSA-PBS. Samples were then incubated in 200ul of anti-BrdU (BD Bioscences, cat #556028) in 1% BSA-PBS for 60 minutes. After a washing step, samples were then incubated in 1 mL propidium iodide (PI) + PBS (Invitrogen, 00-6990-50) with 150ug/mL RNAse A (Qiagen, 19101) overnight at 4°C in the dark. Cell cycle profiles were analyzed by flow cytometry using the Cytoflex SRT (Beckman Coulter).

Immunofluorescence

Cells were fixed in 2% paraformaldehyde at room temperature for 10 min. After fixation, cells were permeabilized with 0.5% Triton X-100 in PBS for 10 min at 4°C, then washed with PBS. Cells were blocked with 1% BSA in PBS at room temperature for 30 min, then incubated with γ-H2AX antibody solution for 1 hour at room temperature. After washing 3 times with PBST, cells were incubated with secondary antibodies conjugated with Cy5 for 1 hour at room temperature, washed with PBST 3 times, and finally mounted with ProLong Diamond Antifade Mountant with DAPI (P36961, Thermo Fisher Scientific). Images were obtained using a Leica DMI6000 (Leica Microsystems).

RNA extraction and quantitative reverse transcription PCR (qRT-PCR)

Total RNA was extracted from cells with the RNeasy Plus Mini kit (Qiagen, cat# 74134) according to the manufacturer's instructions and quantified using Nanodrop or Qubit RNA BR Assay kit on the Qubit 2.0 Fluorometer (Thermo Fisher Scientific). 1000 ng of total RNA was reverse transcribed using SuperScript IV Reverse Transcriptase (Thermo Fisher Scientific, cat # 18090200) and random primers (Promega). RT-qPCR was performed using Power SYBR Green (Life Technologies, cat # 4368708) on a ViiA 7 Real-Time PCR System (Thermo Fisher Scientific). Housekeeping gene PGK1 was used for normalization. All the primer sequences for qRT-PCR are listed in Supplementary Table 1.

cGAMP quantification

cGAMP ELISA were performed according to manufacturer's protocol using Cayman Chemical 2030-cGAMP ELISA Kit (Interchim). ELISA absorbance values were acquired on a CLARIOstar (BMG Labtech) and data were analyzed and exported to Excel with MARS Data Analysis Software (BMG Labtech). For HCT116 AID1 cells, cGAMP quantification was performed on around 3 million cells. Cells were harvested, counted, washed with PBS, pelleted (400 g, 5 mins at 4 °C) and frozen in 500 µl of MeOH/H_2O (80/20, v/v) at -80°C until extraction. Extracts were subjected to five freeze/thaw cycles in liquid nitrogen. The extracts were centrifuged at 16,000 g at 4°C for 20 minutes. The recovered supernatants were subjected to speed vacuum drying in Savant DNA Speed Vac DNA 110 at 65 °C for 2 to 3 hours. The pellets were resuspended in 100 µl of RNase-DNase free water. cGAMP quantities were normalized to the number of cells extracted and represented as pg/million of cells.

Senescence-associated β-galactosidase (SA-β-gal) staining

Senescence-associated β-galactosidase staining was performed with the Senescence Cells Histochemical Staining Kit (Sigma–Aldrich, cat # CS0030-1KT). Briefly, monolayered cells in 6-well plates were incubated with fixation buffer containing 2% formaldehyde for 7 minutes at room temperature, followed by 37°C overnight incubation in staining solution, supplemented with 1 mg/mL of 5-bromo-4-chloro-3-indolyl-β-d-galactopyranoside (X-gal). Plates with staining solution were kept overnight at 37°C without CO_2 until the cells were stained blue. The plates were sealed with parafilm to prevent them from drying out. The stained cell images were taken using LEICA DMi1 (Leica Microsystems).

In vivo experiments

Xenograft Mouse models

Six-week-old Rj:NMRI-Foxn1 nu/nu female mice were acquired from Janvier Labs and maintained under standard conditions (standard diet and water ad libitum) at 23°C with 12h light and 12h dark cycles, in a specific pathogen-free (SPF) animal facility; they were

acclimated a week before performing experiments. To form xenografts, a suspension of HCT116 AID2 cells in 50% Matrigel (Corning #354234) was injected subcutaneously into the right and left flanks of each mouse. Large (L) and small (l) length of each tumor were measured using a caliper and the tumor volume was calculated using the following formula: Volume = ½ ($L \times l^2$). For auxin treatment, we first let the tumors engraft until they reached a volume of approximately 60 mm^3. The mice were injected intraperitoneally daily for 8-10 days with 5-Ph-IAA (3 mg/Kg) or with NaCl 0.9%. Animal work was conducted according to the ethical guidelines applicable in France, in a duly authorized animal facility (Plateforme du Petit Animal du CRCL (P-PAC), agreement number D693880202). Our project received the agreement number APAFIS #49702-202404181412449 v3 from the French Ministry of Education and Research.

Tumor protein extraction

Tumors collected from the xenograft mouse models were cut and placed in a RIPA buffer (R0278 Sigma-Aldrich) with protease inhibitor cocktail (11697498001 Roche) and 0.05% PMSF. Samples were further homogenized using 1.4mm ceramic beads (13113-325, Qiagen) and following the manufacturer's protocol for protein extraction with the Precelley's 24 Dual Lysis and Homogenization (P002511-PEVT0-A.0, Bertin Technologies).

Whole-mount SA-beta-gal staining

At resection, tumors were snap frozen and kept at -80°C until the assay. After thawing, tumors were fixed and Senescence-associated-beta-galactosidase (SA-beta-gal) whole mount staining was performed overnight according to the procedures described in the Senescence Beta-Galactosidase Cell Staining Kit (Cell Signalling #9860). All incubations and washes were performed with fresh and filtered solutions. Stained tissues were then washed twice in PBS and post-fixed with 4% paraformaldehyde before paraffin embedding for sectioning. 8 µm sections were cut and counterstained with Fast Red (Sigma-Aldrich #N30-20-100mL).

Immunohistochemistry (IHC)

Slides were incubated for 15 minutes at 95°C in a solution of deparaffinization and antigen retrieval at pH 6 or pH 9. Then they were rinsed and incubated 20 min at room temperature with primary antibodies (UHRF1 and Ki67). The revelation in brightfield was performed by "Bond Polymer Detection" (Leica DS9800). Sections were lightly counterstained with hematoxylin, then dehydrated and cleared in graded alcohol and Ottix plus (MM-France), and finally covered with glass slips.

RNA sequencing

Sequencing libraries were made from poly-A RNA, as recommended by Illumina, and sequenced using either an Illumina NovaSeq 6000 sequencer in Novogene Co., Ltd. RNA-seq 150bp paired-end reads were assessed for quality using the 'FastQC' algorithm, trimmed as appropriate using the algorithm 'trim-galore' (version 3.0), then the reads were aligned to the human hg38 reference genome using STAR (v2.6.1d). FeatureCounts (v1.5.0-p3) was used to count the read numbers in each gene before differential expression analysis using the linear modeling tool DESeq2 was performed. Using both differential expression methods, significantly changing expression was defined as an adjusted p value (FDR) < 0.05. The expression levels were normalized by transcript per million (TPM) values. Gene ontology analysis was performed using Gene Set enrichment Analysis (GSEA) software (v4.1.0).

Statistical Analysis and visualization

Results were statistically analyzed in GraphPad Prism (version 9.0, GraphPad Software Inc., San Diego, CA) and presented as mean ± SD. Statistically significant differences between two groups were assessed by two-tailed unpaired t-test. Comparisons between two groups were assessed using the unpaired Student's t-test (2-tailed). Comparisons between more than two groups were assessed by one-way ANOVA or Kruskal-Wallis test, followed by multiple comparisons test. $p < 0.05$ was considered significant. ns, not significant; *$p < 0.05$; **$p < 0.01$; ***$p < 0.001$; ****$p < 0.0001$ for indicated comparisons. Statistical details of each experiment can be found in the Results and Figure Legend sections. Principal component analysis (PCA), differentially expressed gene analysis, hierarchical clustering analysis/ heatmap were generated by R software.

Results

Prolonged depletion of DNMT1 and/or UHRF1 triggers senescence in colorectal cancer cell lines

To examine the consequences of prolonged DNA demethylation we used the colorectal cancer cell line HCT116 exploiting the auxin-inducible degron (AID1) system (17). As described in our previous publication (PMID: 38580649), these HCT116 cells express the plant E3 ligase OsTIR1 under a doxycycline (Dox)-inducible promoter, and were edited so that UHRF1, DNMT1, or both, had an AID tag allowing for the proteins of interest to be rapidly degraded in the presence of auxin **(Figure 1A)**. A time-course western blot proved that UHRF1 and/or DNMT1 were completely degraded throughout the duration of the experiment **(Figure 1B)**. To characterize the effect of chronic depletion of UHRF1, DNMT1, or both, we treated the HCT116 derivatives with auxin continuously for 8 days and quantified cell proliferation. The cells depleted of DNMT1 displayed a significant growth defect compared to the WT; this defect was worse in UHRF1-depleted cells, and worst in cells lacking both DNMT1 and UHRF1 **(Figure 1C)**.

To further explore this proliferation defect, we next performed a cell-cycle analysis. HCT116 WT, UHRF1-AID, DNMT1-AID, and UHRF1/DNMT1D-AID cells were collected at time points for up to 8 days after auxin treatment, and stained with BrdU and propidium iodide (PI) to profile the cell cycle proportions **(Figure 1D)**. Through analysis with flow cytometry, we observed a significant decrease in the population of cells in the S phase of the cell cycle after UHRF1 or DNMT1 depletion compared to the WT, which parallels the loss of proliferation seen in the cell growth curve. We also noted a significant accumulation of the cell population in the G1 phase after UHRF1 and/or DNMT1 removal. As G1 phase accumulation is a signature of senescent cells, we hypothesized that UHRF1/DNMT1 depletion may trigger senescence in HCT116 cells.

Senescent cells frequently have large and irregularly shaped nuclei (19). We therefore next analyzed our various conditions after auxin treatment with DAPI staining to determine whether the depletion of UHRF1 or DNMT1 would result in a detectable change in nuclear size and morphology. After analysis with fluorescent microscopy and subsequent quantification, we determined that indeed the loss of UHRF1 and DNMT1 resulted in increased nuclear size, as well as irregular nuclear envelope **(Figure 1E, 1F)**, further suggesting a senescent phenotype in the degron cells.

To further confirm this possible phenotype, we next used an assay to detect the presence of senescence-associated beta galactosidase (SA-beta-gal), a common marker of the increased lysosomal activity present in senescent cells. This experiment revealed a significant increase of SA-beta-gal positive cells after the depletion of DNMT1, which became more pronounced with time. The increase was stronger in cells lacking UHRF1, and strongest in cells lacking both DNMT1 and UHRF1, which parallels their degree of growth impairment **(Figure 1G, 1H)**.

These experiments show that HCT116 cells lacking DNMT1, UHRF1, or both, present 3 phenotypes found in senescent cells: accumulation in G1 phase of the cell cycle; enlargement of the nucleus; and positively stained SA-beta-gal. These data suggest that senescence contributes to the reduced proliferation of cells lacking UHRF1, DNMT1, or both.

Senescence in the depleted cells is linked to loss of DNA methylation and occurs in multiple cellular backgrounds

To determine whether the observations made in HCT116 could be extended to other cellular backgrounds. In our previous publication, we generated auxin-inducible degron alleles of UHRF1 and DNMT1 in colorectal DLD1 cells **(Figure 1I)**, using the AID2 system in which the OsTIR1 activator is 5-Ph-IAA, a derivative of auxin (18). We treated the DLD1 cells with 5-Ph-IAA for 8, 10, or 12 days, then performed SA-beta-gal staining: this revealed a clear increase of SA-beta-gal positivity after the removal of either UHRF1 or DNMT1, extending the link between DNA demethylation and senescence beyond HCT116 cells **(Figure 1J).**

We next asked whether the senescence phenotype seen with the removal of UHRF1 or DNMT1 was specific to the degron system, or if we could confirm it with other means of depletion. For this we treated various cancer cell lines (HCT116, DLD1, HT29, A549, MCF7 and HeLa) with a DNMT1-selective inhibitor GSK3685032 (20) with 640nM for 8 days and 11 days, then performed the SA-beta-gal assay **(Figure 1K)**. We found that the inhibition of DNMT1 led to an increase of SA-beta-gal positive cells in most cell lines, further validating the hypothesis that DNA demethylation induced by UHRF1 or DNMT1 removal triggers senescence, a phenomenon consistent in multiple cancer cell types as well as with various methods of depletion.

Transcriptional profiling of degron cells reveals an interferon response and a SASP signature

Having identified this epigenetically-induced senescence, we moved on to a precise molecular characterization by performing an RNA-seq timed series (0, 2, 4, 6, and 8 days of auxin treatment, **Figure 2A**). These experiments precise and extend the limited transcriptome analysis we previously reported (Days 0 and 4) (PMID: 38580649), yielding important new insight as reported below.

We first computed differentially expressed genes (DEGs) upon UHRF1 and/or DNMT1 depletion over time **(Figure 2B)**. For all degron cells, the number of DEGs increased steadily with time, and there were more upregulated than downregulated genes. The DNMT1 degron cells showed the lowest number of DEGs at all time points, while UHRF1 degron cells had a higher number of DEGs, and the UHRF1/DNMT1 degron cells had the highest number, which parallels both the degree of DNA methylation loss (9) and the prevalence of senescent cells **(Figure 1H)**. There is a high overlap of genes induced by removing UHRF1, DNMT1, or both, consistent with the possibility that they are responding to the loss of DNA methylation **(Figure 2C)**.

We next performed gene set enrichment analysis (GSEA) on our data; a non-exhaustive list of gene sets is shown in **Figure 2D**. Several signatures were downregulated after auxin treatment: those are generally related to cell cycle (E2F targets, MYC targets, cell cycle), which is consistent with the decreased cellular proliferation we observed upon treatment of the degron cells. Conversely, many signatures were upregulated in treated cells, and among them were interferon (IFN) response signatures. This was expected as the interferon response is induced when DNA methylation decreases, after treatment with the DNA demethylating agent such as 5-azacytidine (Aza) and 5-aza-2'-deoxycytidine (Dac) (21, 22), or following RNA interference on DNMT1 or UHRF1 (11, 23). We identified the molecular actors of interferon response by a precise examination of the RNA-seq dataset (**Figure 2E**), this revealed that the cells expressed various IFN receptors at detectable levels (IFNAR1, IFNAR2, IFNGR1, IFNGR2, IFNLR1, IL10Rb), but that the only mRNAs that became clearly induced (IFNL1, IFNL2, IFNL3) encode IFN lambda, a type III IFN. The genes that encode IFN alpha, beta, gamma, kappa, and omega were never expressed at appreciable levels, while the gene for IFN epsilon (IFNE) showed a modest induction at the latest time points. We also verified the presence of an

interferon type III response by RT-qPCR on illustrative genes (IFNL1, IFNL2, IFI27, and ISG15, **Figure 2F**).

The GSEA analysis (**Figure 2D**) showed the induction of a SASP signature containing 125 genes (PMID: 35974106). We refined the SASP signature specific to our system by examining the expression of individual SASP genes (**Figure 2G**). All three degron lines displayed a similar SASP pattern: they induced the same genes encoding cytokines (IL32), chemokines (CCL5), proteases (MMP1, MMP13), growth factors (IGFBP3, IGFBP4), and receptors (ICAM1, TNFRSF1B), a result that was validated by qRT-PCR **(Figure 2H**). This SASP signature was induced fastest and strongest in the double degron UD cells, more slowly and less strongly in the UHRF1 degron cells, and was more delayed and subdued in the DNMT1 degron cells, which again parallels the kinetics of DNA demethylation and senescent phenotypes.

Collectively, our transcriptome data show that the loss of DNA methylation caused by removal of DNMT1, UHRF1, or both, causes HCT116 cells to display a type III interferon response and a SASP signature. This signature is accompanied by activation of different signaling pathways, including p53, therefore we next investigated the determinants of SASP activation and senescence appearance.

DNA demethylation-induced senescence is not accompanied by DNA damage and is independent of p53 and p16/Rb

One of the established triggers of cellular senescence is DNA damage (24). To understand whether the senescence observed in the UHRF1/DNMT1-depleted HCT116 cells may involve DNA damage, we first carried out immunofluorescence on degron cells with an antibody for γ-H2AX, a marker of DNA double-strand breaks **(Figure 3A)**. As a positive control, we treated cells with hydroxyurea (HU), which interferes with DNA replication; this gave rise to a clear γ-H2AX signal, as expected. In contrast, even upon prolonged auxin treatment (8 days), the loss of UHRF1 and/or DNMT1 did not lead to any detectable increase of the γ-H2AX signal. For independent confirmation, we performed a western blot on HCT116 cells after 8 days of auxin treatment **(Figure 3B)**. Two positive controls were used: HU treatment and etoposide treatment, which inhibits Topoisomerase II, also causing double-strand breaks. We tested 4 different actors of the DNA damage response: H2AX, Chk1, Chk2, and p53. All four proteins behaved as anticipated in the positive controls, with increases of γ-H2AX, phospho-Chk1, phospho-Chk2, and p53. In contrast, none of these four markers were induced in the auxin-treated degron cells relative to the auxin-treated WT cells. Altogether these data suggest that DNA damage is unlikely to be a major driver of senescence in the degron cells.

We next investigated the behavior of the p16/Rb pathway. p16 inhibits Cyclin D/CDK complexes, thus preventing the phosphorylation of Rb and entry into S phase. The activation of the p16/Rb pathway is frequently observed in senescent cells.. To test whether this pathway is involved in senescence phenotype observed in the degron cells, we applied an shRNA approach to deplete p16. The WT and degron cells were infected with a lentiviral vector expressing shp16, or the negative control shLuc, then selected to ensure permanent shRNA expression. After these steps, the cells were treated with auxin and we assessed their growth, SA-beta-gal activity, and gene expression pattern by qRT-PCR (**Figure 3C**). The knockdown of p16 did not ameliorate the slow proliferation of degron cells (**Figure 3D**), nor their increased SA-beta-gal positivity (**Figure 3E**). RT-qPCR confirmed sustained suppression of the p16 gene following an 8-day Dox/auxin treatment, yet it did not mitigate SASP gene expression (**Figure 3F**). Collectively, these results indicate that p16 is not a key enforcer of cell cycle arrest or senescence in cells lacking UHRF1 and/or DNMT1.

To further test the contribution of p53 and Rb to senescence in our system, we exploited the oncogenic proteins of human papilloma virus HPV16: E6, that degrades p53, and E7, that inactivates Rb. The WT and degron cells were infected with an empty lentiviral vector, or with a vector expressing E6 and E7, and selected to ensure stable expression **(Figure 3G)**. Although the cell growth curve showed that the U^{AID1} cells coexpressing E6 and E7 grew slightly faster than U^{AID1} control cells, this impact of E6+E7 did not appear in D^{AID1} or UD^{AID1} lines (**Figure 3H**). Additionally, the inactivation of p53 and Rb failed to reduce the SA-beta-gal positivity (**Figure 3I**) or SASP gene expression (**Figure 3J**). Therefore, these results suggest that the senescence observed in HCT116 cells after prolonged DNA demethylation is independent of the p53 and p16/Rb pathways.

Senescence marker p21 is accumulated in cytoplasm and contributes to the anti-apoptosis

Having excluded the role of canonical pathways (p53, p16) in the observed senescence phenotype, we investigated the potential role of other cell cycle-related factors. We first examined the transcriptional pattern of cell cycle-inhibitor encoding genes (CDKN1A, CDKN1B, CDKN2A and CDKN2B) from the RNAseq data and found that similarly to CDKN2A, CDKN1A was also differentially elevated at variouse time points in all the degron lines (**Figure 4A**). CDKN1A encodes p21, which is also a well-known CDK inhibitor binding cyclin-CDK2, cyclin-CDK1, cyclin-CKD4, 6 complexes (25). Notably, CDK2, CDK1 and CDK4 gene expression were downregulated upon Dox/auxin treatment. The genes encoding cyclin E and cyclin A (CCNE1, CCNE2, and CCNA2) were also downregulated (**Figure 4A**). These data parallel the inhibition of cell cycle and also suggest a p21 response in the senescence.

To analyze the potential role of p21 in the degron cell senescence we employed the same strategy as for p16; generating shRNA targeting p21 and assessing the senescence pheotype thruogh various assays (**Figure 4B**). We first monitored cell proliferation after p21 depletion and found that the absence of p21 significantly increased the cell growth of WT cells, but decreased proliferation of U^{AID1} and UD^{AID1} lines (**Figure 4C**), indicating that the loss of p21 may reduce the viability of senescent cells.

A primary characteristic of senescent cells is their capacity to resist apoptosis (26). CDKN1A/p21 has diverse functions depending on its subcellular localization (25). Nuclear p21 plays a role in anti-proliferation, while cytoplasmic p21 contrarily contributes to pro-survival pathways by suppressing JNK and caspase signaling; its knockdown has been shown to induce apoptosis in senescent cells (27). We next performed a cellular fractionation in the HCT116 cells after 8 days of auxin treatment to see in which cellular compartment p21 was accumulating after the depletion of UHRF1 and/or DNMT1. Strikingly, the western blot results revealed an aggregation of p21 in the cytoplasm upon UHRF1/DNMT1 knockdown (**Figure 4D**), consistent with previous studies indicating cytosolic p21's role in anti-apoptosis during senescence.

Analyzing further the dynamics of anti-apoptotic regulators in HCT116 senescent cells, we checked the protein levels of various apoptosis factors such as H2AX, rH2AX, PARP (full-length and cleaved) after p21 knockdown with a western blot. The results revealed an increase of DNA damage marker γ-H2AX, as well as the presence of cleaved poly ADP-Ribose Polymerase (PARP), a sign of apoptosis (**Figure 4E**). We next performed an Annexin V assay to assess the level of apoptosis in our cells after the knockdown of p21. We posited that if cytosolic p21 is truly responsible for the anti-apoptotic phenotype seen in our senescent cells, then its knockdown should increase the amount of Annexin V binding: indicating apoptosis. Compared to the control conditions, the loss of p21 led to an increase of apoptosis in the

conditions depleted for UHRF1 and/or DNMT1 (**Figure 4F, 4G**), highlighting the role of p21 in the upregulation of anti-apoptotic factors during senescence in HCT116 cells after chronic DNA demethylation.

SA-beta-gal staining revealed that p21 knockdown lead to a partial reduction of SA-beta-gal positivity (**Figure 4H, 4I**), but no significant effect on overall SASP expression (**Figure 4J**). These data suggest that while p21 is not a mediator of the SASP expression, it contributes to the increased lysosomal content observed in the senescence phenotype.

Collectively, p21 plays a non-canonical function in senescent HCT116 lacking UHRF1/DNMT1. Knockdown of p21 upon UHRF1/DNMT1 depletion not only attenuates the pro-survival pathway and triggers apoptosis in HCT116 senescent cells, but also alleviates the augmented lysosomal content.

Noncanonical cGAS activation contributes to the SASP response and lysosomal activity of senescent cells

Apart from the canonical pathways, cellular senescence can also be triggered by other pathways, including the nuclear acid sensor pathway cGAS/STING. cGAS/STING initially emerges as a central node modulating innate immune response, but accumulating studies have reported its role in cumulative senescence and SASP-derived inflammation. Our GSEA analysis (**Figure 2D**) showed upregulated cytosolic DNA sensing signature in degron lines upon UHRF1 or DNMT1 depletion, prompting us to consider whether the cGAS/STING pathway plays a role in HCT116 senescent cells.

To delineate the potential role of the cGAS/STING pathway we first performed RT-qPCR on the HCT116 cells at various timepoints after auxin treatment to measure the expression of cGAS. Notably, cGAS is highly suppressed in HCT116 WT cells. The results showed that the loss of UHRF1 and DNMT1 together triggered a dramatic upregulation of cGAS; this was less prominent after UHRF1 depletion and not significant after DNMT1 loss (**Figure 5A**). We further validated this with western blot, showing the continued increase of cGAS expression over time, particularly in the UD^{AID1} line (**Figure 5B**).

In mammalian cells, the enzyme cGAS produces the cyclic dinucleotide 2',3'-cyclic GMP-AMP (cGAMP). To assess the enzymatic activation of induced cGAS in our degron lines, we performed ELISA to detect cGAMP. Surprisingly, the amount of cGAMP increased at early time points and then declined at the later time points (**Figure 5C**). cGAS senses double-stranded DNA within the cytoplasm and exerts its enzymatic role; a possible explanation for the wave change of cGAMP could be the change of cGAS subcellular location. To verify the hypothesis of cGAS translocation, we performed a cellular fractionation and observed that cGAS protein was accumulated in the nuclear fraction (**Figure 5D**).

To better understand the role of induced cGAS during senescence, we performed a knockdown using shRNA targeting either a scrambled sequence or cGAS to observe the effect on senescence phenotype upon Dox/auxin treatment (**Figure 5E**). A cell growth curve revealed no significant effect of cGAS knockdown on slow cell proliferation (**Figure 5F**). However, the results of the SA-beta-gal assay showed a noticeable decrease in lysosomal activity in the conditions of cGAS knockdown compared to the control, suggesting cGAS may contribute to the increased lysosomal activity of the observed senescence phenotype (**Figure 5G**). qRT-PCR analysis confirmed the continuous suppression of cGAS after knockdown, and also revealed a downregulation of the SASP genes that are typically induced after DNMT1/UHRF1 depletion, suggesting that cGAS activation contributes to the SASP gene induction (**Figure 5H**).

STING has been frequently functionally suppressed in human cancers (28), therefore, we examined the presence of cGAS and STING in different cancer cells that we used for DNMT1 inhibitor treatment. As expected, these cells exhibited varying levels of disrupted cGAS or STING activity (**Figure 5I**), indicating that the DNA demethylation-induced senescence may not be dependent on the cGAS/STING canonical function. To further evaluate the role of STING in senescence, we employed CRISPR/cas9 to knockout STING in the degron cells and then assessed the senescence phenotype (**Figure 5J**). We first confirmed efficiency of the STING knockout after 8 days of dox/auxin treatment, as well as the absence of impact on SASP gene expression after STING loss (**Figure 5K**). SA-beta-gal staining showed no significant impact of lysosomal activity after STING loss (**Figure 5L**),

Collectively, these results indicate that the induction of cGAS after chronic DNA methylation loss after UHRF1/DNMT1 depletion contributes to the activation of SASP genes and increased lysosomal activity, and this contribution is independent of STING.

Prolonged DNA demethylation also triggers cancer senescence in vivo

Through a multitude of experiments, our results clearly established that the depletion of UHRF1 and/or DNMT1 triggers senescence in not only HCT116 cells, but other cancer cell lines as well. We next sought to confirm if this was an event also reproducible *in vivo*. For this, we used the AID2 system in HCT116 cells, in which a much lower concentration of 5-Ph-IAA is sufficient to degrade the AID-tagged protein of interest *in vitro* and *in vivo*. We generated and validated HCT116 expressing OsTIR1(F47G) and its derivatives (U^{AID2}, D^{AID2} and UD^{AID2}) (**Figure 6A**). Cells from each condition (HCT116 WT^{F47G}, U^{AID2}, D^{AID2} and UD^{AID2}) were transplanted into both flanks of a nude mouse, which formed xenograft tumors after 7 days. We then administered either PBS or 3 mg/kg of 5-Ph-IAA via intraperitoneal (i.p.) injections daily for an additional 8 to 10 days. At the end of the experiment the mice were sacrificed, and tumors were resected to make a series of biological assessments (**Figure 6B**).

We first sought to confirm the *in vivo* success of the AID degradation system. Upon extracting protein from frozen tumor samples and conducting a western blot, we found that UHRF1 or DNMT1 was detectable in the PBS control group but entirely absent following 5-Ph-IAA treatment (**Figure 6C**). We also performed immunohistochemistry (IHC) of UHRF1 and observed a significant reduction of UHRF1 in U^{AID2} and UD^{AID2} xenografts but not in WT^{F47G} and D^{AID2} xenograft upon 5-Ph-IAA treatment (**Figure 6D, 6E**), thereby affirming the system's effectiveness in vivo.

Consistent with our in vitro findings, UHRF1 and/or DNMT1 xenografts showed a decreased signal of Ki67, a proliferative indicator, in degron xenografts compared to WT xenograft upon treatment (**Figure 6F**), indicating a cell proliferation defect as seen in senescent cells. The control group of tumors showed little variation in tumor weight amongst the four xenograft conditions, however we observed a significant tumor suppression of U^{AID2} xenograft and relatively decreased tumor weight of D^{AID2} and UD^{AID2} xenografts upon 5-Ph-IAA treatment, indicating that the loss of UHRF1/ DNMT1 arrests tumor growth (**Figure 6G**).

To confirm whether the decrease in tumor size results from senescence triggered by the degradation, we performed whole-mount SA-beta-gal assay to detect the accumulation of cell senescence on the entire tumors. After fixing and staining, tumor sections were counterstained with Nuclear Fast Red. Strikingly, the results revealed a dramatic increase of SA-beta-gal positivity in U^{AID2} and UD^{AID2} xenografts, with a moderate increase of SA-beta-gal positivity in D^{AID2} xenograft upon treatment (**Figure 6H, 6I**), further validating the assertion that the depletion of these factors indeed triggers senescence.

Discussion

Using powerful degron tools, we have observed a time-course cellular response in the context of chronic DNA demethylation in cancer cells. A paramount outcome of this work is finding the inhibition DNMT1 or UHRF1 renders cancer cells senescent without provoking DNA damage. Importantly, our research reveals that this strategy prevails even in tumors lacking functional p16, p53, or Rb. Through this work we also reveal that this DNA demethylation-induced senescence is accompanied by non-canonical functions of p21 and cGAS, proving further insight into mechanisms of senescence as well as potential for improving human cancer treatments.

DNA-demethylation induced senescence in not a canonical senescence

Cellular senescence is traditionally defined as a permanent cell cycle arrest triggered by stress or damage, leading to various intracellular phenotypic alterations. Canonical senescence has many hallmarks including cell cycle arrest, DNA damage response activation, nuclear changes, anti-apoptotic factors upregulation, SASP, increased lysosomal content, metabolic adaptations, elevated expression of senescence-associated protein or glycan receptors on the cell surface and changes in morphology (29). Our study details a different type of senescence: one that is triggered by chronic DNA demethylation. While this senescence exhibits several canonical senescence markers, including enlarged nuclear size, G1 cell cycle arrest, increased SA-beta-gal activity, and SASP response, it is not accompanied by detectable DNA damage and functions independently of p53, p16, and pRB (retinoblastoma).

DNA damage is a well-established trigger of many types of senescence, including replicative senescence, oncogene-induced senescence, and therapy-induced senescence (30, 31). Double-strand breaks trigger the DNA damage response (DDR), a signaling cascade centered around the ataxia teleangectasia-mutated (ATM) kinase that activates p53 to elicit cell-cycle arrest and to induce senescence (32). However, the absence of DDR was also described in another type of senescence induction in nonproliferating (33) and proliferating cells (34). 5-aza-2'-deoxycytidine can also induce senescence without DNA damage accumulation in leukemia cells (15). In our case, by checking the DNA damage response factors, we could not find a significant increase of DDR in the senescence triggered by DNA demethylation. Pathway investigation also showed that p53 degradation failed to impact the senescence phenotype. Senescence induced through DNMT1 inhibition in different cancer cell lines with or without a mutated p53 background also proved that p53 is not indispensable for this senescence. p53 is mutated in over 50% of human cancers (35), and tumor cells containing mutated p53 typically display stronger resistance to anticancer agents (36). Our results pave the way for targeting UHRF1 function in these cells to render them senescent and halt tumor growth.

Compared to the senescence triggered by DNA damage, it is likely that epigenetic modifiers directly trigger senescence by transcriptionally activating repressed loci (like p16), therefore without generating detectable cell stress (30). In canonical senescence, the p16-mediated senescence acts through the pRb pathway, inhibiting the action of the cyclin-dependent kinases and leading to G1 cell cycle arrest. Rb is maintained in a hypophosphorylated state, resulting in the inhibition of transcription factor E2F1. Regulation of p16 expression is complex and involves both epigenetic control and multiple transcription factors. p16 has been confirmed to be heterozygously methylated in HCT116 cells (37, 38);

therefore, apart from the p53 pathway, p16 is another strong possibility for inducing senescence in our context. We have indeed observed an increased p16 expression upon UHRF1 or DNMT1 depletion (data not shown), but we proved that p16 alone is not required for establishing or maintaining this senescence. Moreover, the use of a DNMT1 inhibitor can trigger senescence in p16 homozygously depleted cell lines (A549, MCF7) (39), reinforcing our conclusion that this senescence is independent of p16.

The role of p21 in this non canonical senescence

p21 functions within the nucleus as a cell proliferation inhibitor by binding to cyclin/CDK complexes (40, 41) and proliferating cell nuclear antigen (PCNA) (42), and is thereby implicated in senescence growth arrest. Interestingly, our model shows p21 accumulation primarily in the cytoplasm of UHRF1 or DNMT1-depleted cells, suggesting that the induction of p21 does not regulate the cell cycle, and its function depends on p53. Our work demonstrates that p21 knockdown impacts the viability of senescent cells, increasing the proportion of apoptotic cells. Previous reports have shown that silencing p21 expression through siRNA induces apoptosis in other senescence types, similar to doxorubicin-induced senescence (43). Though the mechanism of how p21 acts as an anti-apoptosis regulator in our senescence model is unclear, the data suggest that eliminating senescent cells via inhibition of p21 is a promising strategy for targeting senescent cancer cells. As previously identified, cytoplasmic p21 could exhibit anti-apoptotic activity owing to the inhibition of proteins involved in apoptosis including procaspase-3, SAPK (stress-activated protein kinase), and ASK1 (apoptosis signal-regulated kinase 1) (25, 44). Further research is required to define the mode of cell death and the mechanisms induced in senescent cells after knockdown of p21.

In addition to identifying the anti-apoptotic role of p21 in our senescence model, we also observed that p21 expression contributes to the increased lysosomal content as demonstrated in the SA-beta-gal staining assays. P21 knockdown cells exhibited decreased SA-beta-gal positivity, however SASP gene expression revealed no significant alleviation, suggesting that p21 is unlikely to be upstream of the SASP response, and rather directly or indirectly targets the function related to the lysosomal activity in senescent cells. It has been demonstrated that increased SA-beta-gal staining reflects increased lysosomal content and increased autophagy flux (45). Autophagy is an evolutionarily conserved cellular process in which macromolecules undergo lysosomal degradation. Autophagic activity is up-regulated in oncogene induced senescence (46). It has also been reported that overexpression of CDK inhibitors including p21 activates autophagy and cellular senescence in both human fibroblasts and breast cancer cells (47), leading us to speculate that p21 might be involved in the process of autophagy in senescence, which also needs to be validated in the future. Currently our data strongly suggests that p21 is one of the master regulators of DNA demethylation-induced senescence by controlling several molecular pathways.

More context regarding the upregulation of p21 in DNA demethylation-induced senescence remains to be clarified. The expression of p21 can be regulated by several epigenetic factors and other post-transcriptional mechanisms which are interconnected together (48). Previous studies showed that Cdkn1a (encoding p21) expression goes up in uhrf1-deficient immune cells (49, 50); however, the affected demethylated sites of Cdkn1a are controversial. DNA hypermethylation and the consequent silencing of p21 have been noted in numerous cancers (51). However, it has also been reported that in the A549 cell line,

DNMT inhibition can upregulate p21 without involving promoter DNA methylation (52). In our study, p21 does not appear to be directly regulated by DNA demethylation, as indicated by RNAseq data that reveals fluctuating CDKN1A transcription over time. This suggests that other factors like MYC and AP4, previously studied (53–55), may influence p21 expression. Additional research is needed to clarify this regulation.

The role of cGAS in this non canonical senescence

As a DNA sensor, cGAS has been well recognized for its classic biological function in innate immunity. Recent evidence has revealed that the cGAS-STING pathway is robustly implicated in cellular senescence. Binding with accumulated self-derived DNA fragments in senescent cells, cGAS can activate downstream of NF-κB or IRF3 transcription factors to trigger SASP production in either normal or cancer senescent cells (56–62). In line with these reports, our study shows that cGAS is important for the increased lysosomal mass and the induction of the SASP response in our cancer cell models. Intriguingly, our data suggests that cGAS mediates the SASP response independently of STING.

A possible explanation is that many cancer cells fail to express cGAS or STING, rendering the proteins functionally silent (28, 63). For example, HCT116 and DLD-1 cells have transcriptionally silenced cGAS, whileA549 cell lines lack STING expression. Some cancers cells express STING which has impaired ability to activate transcription factors NF-kB or IRF3E (28). Although cGAS is derepressed in the context of DNA demethylation, it is possible to be STING independent.

An alternative explanation is the subcellular localization of cGAS in the nucleus shown in our model. Based on current knowledge, only cytosolic cGAS regulates SASP response, making our study the first to link nuclear cGAS function to mediating SASP in senescent cells. There are numerous studies showing various functions of cGAS in the nucleus, including the regulation of DNA damage repair, nuclear membrane restoration, chromosome fusion, DNA replication and angiogenesis among other non-traditional functions (PMID: 38515746). It is still unclear that how cGAS regulates SASP in nucleus, but a recent study discovered that chromatin-bound cGAS can recruit the SWI/SNF complex at specific chromatin regions to regulate gene expression (64), leading us to hypothesize that the nuclear cGAS in our model may also recruit similar mediator and contribute to the SASP gene expression, though further studies must be carried out to verify this.

SASP factors can exert both beneficial and deleterious functions (65). The SASP signature in our context includes many deleterious and pro-tumorigenesis factors, such as MMP1, MMP13. Based on the role of cGAS in facilitating SASP induction, modulation of its activity would be beneficial for inhibit cancer development.

Acknowledgments

Work in the lab of PAD is supported by Agence Nationale de la Recherche, Institut National du Cancer, and Fondation pour la Recherche Médicale. This study was also supported by the LabEx “Who Am I?” #ANR-11-LABX-0071 and the Université de Paris IdEx #ANR-18-IDEX-0001 funded by the French Government through its “Investments for the Future” program. XC received support from "Fondation pour la Recherche Médicale" for the last year of her PhD. KY was supported by ARC foundation CDD Post-doctorant en France (Ref. No. PDF20181208337), Labex "Who Am I?" postdoctoral support, and a JSPS Postdoctoral Fellowship for Research Abroad (Ref. No. 202260432). The work of FM and TI was supported by Research Support Project for Life Science and Drug Discovery (Basis for Supporting Innovative Drug Discovery and Life Science Research (BINDS)) from AMED under Grant Number JP23ama121022. The authors are grateful to the Hist'IM facility of Institut Cochin and ImagoSeine core facility of Institut Jacques Monod, member of France-BioImaging (ANR-10-INBS-04), with the support of Plan Cancer, Region Ile-de-France and Fondation Bettencourt Schueller (R03/75-79). We also thank the Vectorology platform, Epigenetics platform, Microscopy platform and Bioinformatics/Biostatistics Core Facility (BIBS) at the CNRS Epigenetics and Cell Fate Unit (Université Paris Cité), for providing access and technical advice.

We are very grateful to Saadi Khochbin, Allison Bardin, Gael Cristofari, Corinne Abadie, Bill Keyes, Julien Cherfils-Vicini, Vjekoslav Dulic, Clément Hua, Han Li, Raphael Margueron, François Radvanyi, Laurent Reber, David Roulois for useful advice. We thank the following colleagues for the gift of useful reagents: Fadila Rayah and Catherine Postic, Emma Lamana and Pierre Bruhns.

Competing interests statement

The authors declare no competing financial interests.

References

1. Li,E. and Zhang,Y. (2014) DNA methylation in mammals. *Cold Spring Harb Perspect Biol*, **6**, a019133.

2. Laisné,M., Gupta,N., Kirsh,O., Pradhan,S. and Defossez,P.-A. (2018) Mechanisms of DNA Methyltransferase Recruitment in Mammals. *Genes (Basel)*, **9**.

3. Petryk,N., Bultmann,S., Bartke,T. and Defossez,P.-A. (2020) Staying true to yourself: mechanisms of DNA methylation maintenance in mammals. *Nucleic Acids Res*, 10.1093/nar/gkaa1154.

4. Schübeler,D. (2015) Function and information content of DNA methylation. *Nature*, **517**, 321–326.

5. Sharp,A.J., Stathaki,E., Migliavacca,E., Brahmachary,M., Montgomery,S.B., Dupre,Y. and Antonarakis,S.E. (2011) DNA methylation profiles of human active and inactive X chromosomes. *Genome Res*, **21**, 1592–1600.

6. Dawson,M.A. (2017) The cancer epigenome: Concepts, challenges, and therapeutic opportunities. *Science*, **355**, 1147–1152.

7. Bostick,M., Kim,J.K., Estève,P.-O., Clark,A., Pradhan,S. and Jacobsen,S.E. (2007) UHRF1 plays a role in maintaining DNA methylation in mammalian cells. *Science*, **317**, 1760–1764.

8. Sharif,J., Muto,M., Takebayashi,S., Suetake,I., Iwamatsu,A., Endo,T.A., Shinga,J., Mizutani-Koseki,Y., Toyoda,T., Okamura,K., *et al.* (2007) The SRA protein Np95 mediates epigenetic inheritance by recruiting Dnmt1 to methylated DNA. *Nature*, **450**, 908–912.

9. Yamaguchi,K., Chen,X., Rodgers,B., Miura,F., Bashtrykov,P., Bonhomme,F., Salinas-Luypaert,C., Haxholli,D., Gutekunst,N., Aygenli,B.Ö., *et al.* (2024) Non-canonical functions of UHRF1 maintain DNA methylation homeostasis in cancer cells. *Nat Commun*, **15**, 2960.

10. Mudbhary,R., Hoshida,Y., Chernyavskaya,Y., Jacob,V., Villanueva,A., Fiel,M.I., Chen,X., Kojima,K., Thung,S., Bronson,R.T., *et al.* (2014) UHRF1 overexpression drives DNA hypomethylation and hepatocellular carcinoma. *Cancer Cell*, **25**, 196–209.

11. Kong,X., Chen,J., Xie,W., Brown,S.M., Cai,Y., Wu,K., Fan,D., Nie,Y., Yegnasubramanian,S., Tiedemann,R.L., *et al.* (2019) Defining UHRF1 Domains that Support Maintenance of Human Colon Cancer DNA Methylation and Oncogenic Properties. *Cancer Cell*, **35**, 633-648.e7.

12. Zhang,X., Li,B., de Jonge,N., Björkholm,M. and Xu,D. (2015) The DNA methylation inhibitor induces telomere dysfunction and apoptosis of leukemia cells that is attenuated by telomerase over-expression. *Oncotarget*, **6**, 4888–4900.

13. Venturelli,S., Berger,A., Weiland,T., Essmann,F., Waibel,M., Nuebling,T., Häcker,S., Schenk,M., Schulze-Osthoff,K., Salih,H.R., *et al.* (2013) Differential induction of apoptosis and senescence by the DNA methyltransferase inhibitors 5-azacytidine and 5-aza-2'-deoxycytidine in solid tumor cells. *Mol Cancer Ther*, **12**, 2226–2236.

14. Patra,A., Deb,M., Dahiya,R. and Patra,S.K. (2011) 5-Aza-2'-deoxycytidine stress response and apoptosis in prostate cancer. *Clin Epigenetics*, **2**, 339–348.

15. Grandjenette,C., Schnekenburger,M., Karius,T., Ghelfi,J., Gaigneaux,A., Henry,E., Dicato,M. and Diederich,M. (2014) 5-aza-2'-deoxycytidine-mediated c-myc Down-regulation triggers telomere-dependent senescence by regulating human telomerase reverse transcriptase in chronic myeloid leukemia. *Neoplasia*, **16**, 511–528.

16. Amatori,S., Bagaloni,I., Viti,D. and Fanelli,M. (2011) Premature senescence induced by DNA demethylating agent (Decitabine) as therapeutic option for malignant pleural mesothelioma. *Lung Cancer*, **71**, 113–115.

17. Natsume,T., Kiyomitsu,T., Saga,Y. and Kanemaki,M.T. (2016) Rapid Protein Depletion in Human Cells by Auxin-Inducible Degron Tagging with Short Homology Donors. *Cell Rep*, **15**, 210–218.

18. Yesbolatova,A., Saito,Y., Kitamoto,N., Makino-Itou,H., Ajima,R., Nakano,R., Nakaoka,H., Fukui,K., Gamo,K., Tominari,Y., *et al.* (2020) The auxin-inducible degron 2 technology provides sharp degradation control in yeast, mammalian cells, and mice. *Nat Commun*, **11**.

19. Tsai,C.-H., Chang,C.-Y., Lin,B.-Z., Wu,Y.-L., Wu,M.-H., Lin,L.-T., Huang,W.-C., Holz,J.D., Sheu,T.-J., Lee,J.-S., *et al.* (2021) Up-regulation of cofilin-1 in cell senescence associates with morphological change and p27kip1 -mediated growth delay. *Aging Cell*, **20**, e13288.

20. Pappalardi,M.B., Keenan,K., Cockerill,M., Kellner,W.A., Stowell,A., Sherk,C., Wong,K., Pathuri,S., Briand,J., Steidel,M., *et al.* (2021) Discovery of a first-in-class reversible DNMT1-selective inhibitor with improved tolerability and efficacy in acute myeloid leukemia. *Nat Cancer*, **2**, 1002–1017.

21. Roulois,D., Loo Yau,H., Singhania,R., Wang,Y., Danesh,A., Shen,S.Y., Han,H., Liang,G., Jones,P.A., Pugh,T.J., *et al.* (2015) DNA-Demethylating Agents Target Colorectal Cancer Cells by Inducing Viral Mimicry by Endogenous Transcripts. *Cell*, **162**, 961–973.

22. Chiappinelli,K.B., Strissel,P.L., Desrichard,A., Li,H., Henke,C., Akman,B., Hein,A., Rote,N.S., Cope,L.M., Snyder,A., *et al.* (2015) Inhibiting DNA Methylation Causes an Interferon Response in Cancer via dsRNA Including Endogenous Retroviruses. *Cell*, **162**, 974–986.

23. Cai,Y., Tsai,H.-C., Yen,R.-W.C., Zhang,Y.W., Kong,X., Wang,W., Xia,L. and Baylin,S.B. (2017) Critical threshold levels of DNA methyltransferase 1 are required to maintain

DNA methylation across the genome in human cancer cells. *Genome Res.*, **27**, 533–544.

24. Ogrodnik,M., Carlos Acosta,J., Adams,P.D., d'Adda di Fagagna,F., Baker,D.J., Bishop,C.L., Chandra,T., Collado,M., Gil,J., Gorgoulis,V., *et al.* (2024) Guidelines for minimal information on cellular senescence experimentation in vivo. *Cell*, **187**, 4150–4175.

25. Abbas,T. and Dutta,A. (2009) p21 in cancer: intricate networks and multiple activities. *Nat Rev Cancer*, **9**, 400–414.

26. Soto-Gamez,A., Quax,W.J. and Demaria,M. (2019) Regulation of Survival Networks in Senescent Cells: From Mechanisms to Interventions. *J Mol Biol*, **431**, 2629–2643.

27. Yosef,R., Pilpel,N., Papismadov,N., Gal,H., Ovadya,Y., Vadai,E., Miller,S., Porat,Z., Ben-Dor,S. and Krizhanovsky,V. (2017) p21 maintains senescent cell viability under persistent DNA damage response by restraining JNK and caspase signaling. *EMBO J*, **36**, 2280–2295.

28. Xia,T., Konno,H., Ahn,J. and Barber,G.N. (2016) Deregulation of STING Signaling in Colorectal Carcinoma Constrains DNA Damage Responses and Correlates With Tumorigenesis. *Cell Rep*, **14**, 282–297.

29. Suryadevara,V., Hudgins,A.D., Rajesh,A., Pappalardo,A., Karpova,A., Dey,A.K., Hertzel,A., Agudelo,A., Rocha,A., Soygur,B., *et al.* (2024) SenNet recommendations for detecting senescent cells in different tissues. *Nat Rev Mol Cell Biol*, 10.1038/s41580-024-00738-8.

30. Petrova,N.V., Velichko,A.K., Razin,S.V. and Kantidze,O.L. (2016) Small molecule compounds that induce cellular senescence. *Aging Cell*, **15**, 999–1017.

31. Di Micco,R., Krizhanovsky,V., Baker,D. and d'Adda di Fagagna,F. (2021) Cellular senescence in ageing: from mechanisms to therapeutic opportunities. *Nat Rev Mol Cell Biol*, **22**, 75–95.

32. Rufini,A., Tucci,P., Celardo,I. and Melino,G. (2013) Senescence and aging: the critical roles of p53. *Oncogene*, **32**, 5129–5143.

33. Alimonti,A., Nardella,C., Chen,Z., Clohessy,J.G., Carracedo,A., Trotman,L.C., Cheng,K., Varmeh,S., Kozma,S.C., Thomas,G., *et al.* (2010) A novel type of cellular senescence that can be enhanced in mouse models and human tumor xenografts to suppress prostate tumorigenesis. *J Clin Invest*, **120**, 681–693.

34. Prieur,A., Besnard,E., Babled,A. and Lemaitre,J.-M. (2011) p53 and p16(INK4A) independent induction of senescence by chromatin-dependent alteration of S-phase progression. *Nat Commun*, **2**, 473.

35. Baugh,E.H., Ke,H., Levine,A.J., Bonneau,R.A. and Chan,C.S. (2018) Why are there hotspot mutations in the TP53 gene in human cancers? *Cell Death Differ*, **25**, 154–160.

36. Beckta,J.M., Ahmad,S.F., Yang,H. and Valerie,K. (2014) Revisiting p53 for cancer-specific chemo- and radiotherapy: ten years after. *Cell Cycle*, **13**, 710–713.

37. Rhee,I., Jair,K.W., Yen,R.W., Lengauer,C., Herman,J.G., Kinzler,K.W., Vogelstein,B., Baylin,S.B. and Schuebel,K.E. (2000) CpG methylation is maintained in human cancer cells lacking DNMT1. *Nature*, **404**, 1003–1007.

38. Burri,N., Shaw,P., Bouzourene,H., Sordat,I., Sordat,B., Gillet,M., Schorderet,D., Bosman,F.T. and Chaubert,P. (2001) Methylation silencing and mutations of the p14ARF and p16INK4a genes in colon cancer. *Lab Invest*, **81**, 217–229.

39. Herman,J.G., Merlo,A., Mao,L., Lapidus,R.G., Issa,J.P., Davidson,N.E., Sidransky,D. and Baylin,S.B. (1995) Inactivation of the CDKN2/p16/MTS1 gene is frequently associated with aberrant DNA methylation in all common human cancers. *Cancer Res*, **55**, 4525–4530.

40. Xiong,Y., Hannon,G.J., Zhang,H., Casso,D., Kobayashi,R. and Beach,D. (1993) p21 is a universal inhibitor of cyclin kinases. *Nature*, **366**, 701–704.

41. Harper,J.W., Adami,G.R., Wei,N., Keyomarsi,K. and Elledge,S.J. (1993) The p21 Cdk-interacting protein Cip1 is a potent inhibitor of G1 cyclin-dependent kinases. *Cell*, **75**, 805–816.

42. Waga,S., Hannon,G.J., Beach,D. and Stillman,B. (1994) The p21 inhibitor of cyclin-dependent kinases controls DNA replication by interaction with PCNA. *Nature*, **369**, 574–578.

43. Sikora,E., Mosieniak,G. and Sliwinska,M.A. (2016) Morphological and Functional Characteristic of Senescent Cancer Cells. *Curr Drug Targets*, **17**, 377–387.

44. Moussa,R.S., Park,K.C., Kovacevic,Z. and Richardson,D.R. (2019) Ironing out the role of the cyclin-dependent kinase inhibitor, p21 in cancer: Novel iron chelating agents to target p21 expression and activity. *Free Radic Biol Med*, **133**, 276–294.

45. Ashraf,H.M., Fernandez,B. and Spencer,S.L. (2023) The intensities of canonical senescence biomarkers integrate the duration of cell-cycle withdrawal. *Nat Commun*, **14**, 4527.

46. Young,A.R.J., Narita,M., Ferreira,M., Kirschner,K., Sadaie,M., Darot,J.F.J., Tavaré,S., Arakawa,S., Shimizu,S., Watt,F.M., *et al.* (2009) Autophagy mediates the mitotic senescence transition. *Genes Dev*, **23**, 798–803.

47. Capparelli,C., Chiavarina,B., Whitaker-Menezes,D., Pestell,T.G., Pestell,R.G., Hulit,J., Andò,S., Howell,A., Martinez-Outschoorn,U.E., Sotgia,F., *et al.* (2012) CDK inhibitors (p16/p19/p21) induce senescence and autophagy in cancer-associated fibroblasts, 'fueling' tumor growth via paracrine interactions, without an increase in neo-angiogenesis. *Cell Cycle*, **11**, 3599–3610.

48. Ocker,M., Bitar,S.A., Monteiro,A.C., Gali-Muhtasib,H. and Schneider-Stock,R. (2019) Epigenetic Regulation of p21cip1/waf1 in Human Cancer. *Cancers (Basel)*, **11**, 1343.

49. Chen,C., Zhai,S., Zhang,L., Chen,J., Long,X., Qin,J., Li,J., Huo,R. and Wang,X. (2018) Uhrf1 regulates germinal center B cell expansion and affinity maturation to control viral infection. *J Exp Med*, **215**, 1437–1448.

50. Obata,Y., Furusawa,Y., Endo,T.A., Sharif,J., Takahashi,D., Atarashi,K., Nakayama,M., Onawa,S., Fujimura,Y., Takahashi,M., *et al.* (2014) The epigenetic regulator Uhrf1 facilitates the proliferation and maturation of colonic regulatory T cells. *Nat Immunol*, **15**, 571–579.

51. Kreis,N.-N., Louwen,F. and Yuan,J. (2019) The Multifaceted p21 (Cip1/Waf1/CDKN1A) in Cell Differentiation, Migration and Cancer Therapy. *Cancers (Basel)*, **11**, 1220.

52. Milutinovic,S., Knox,J.D. and Szyf,M. (2000) DNA methyltransferase inhibition induces the transcription of the tumor suppressor p21(WAF1/CIP1/sdi1). *J Biol Chem*, **275**, 6353–6359.

53. Jackstadt,R., Röh,S., Neumann,J., Jung,P., Hoffmann,R., Horst,D., Berens,C., Bornkamm,G.W., Kirchner,T., Menssen,A., *et al.* (2013) AP4 is a mediator of epithelial-mesenchymal transition and metastasis in colorectal cancer. *J Exp Med*, **210**, 1331–1350.

54. Jung,P., Menssen,A., Mayr,D. and Hermeking,H. (2008) AP4 encodes a c-MYC-inducible repressor of p21. *Proc Natl Acad Sci U S A*, **105**, 15046–15051.

55. Seoane,J., Le,H.-V. and Massagué,J. (2002) Myc suppression of the p21(Cip1) Cdk inhibitor influences the outcome of the p53 response to DNA damage. *Nature*, **419**, 729–734.

56. Yang,H., Wang,H., Ren,J., Chen,Q. and Chen,Z.J. (2017) cGAS is essential for cellular senescence. *Proc Natl Acad Sci U S A*, **114**, E4612–E4620.

57. Dou,Z., Ghosh,K., Vizioli,M.G., Zhu,J., Sen,P., Wangensteen,K.J., Simithy,J., Lan,Y., Lin,Y., Zhou,Z., *et al.* (2017) Cytoplasmic chromatin triggers inflammation in senescence and cancer. *Nature*, **550**, 402–406.

58. De Cecco,M., Ito,T., Petrashen,A.P., Elias,A.E., Skvir,N.J., Criscione,S.W., Caligiana,A., Brocculi,G., Adney,E.M., Boeke,J.D., *et al.* (2019) L1 drives IFN in senescent cells and promotes age-associated inflammation. *Nature*, **566**, 73–78.

59. Liu,X., Liu,Z., Wu,Z., Ren,J., Fan,Y., Sun,L., Cao,G., Niu,Y., Zhang,B., Ji,Q., *et al.* (2023) Resurrection of endogenous retroviruses during aging reinforces senescence. *Cell*, **186**, 287-304.e26.

60. Loo,T.M., Miyata,K., Tanaka,Y. and Takahashi,A. (2020) Cellular senescence and senescence-associated secretory phenotype via the cGAS-STING signaling pathway in cancer. *Cancer Sci*, **111**, 304–311.

61. Wu,Q., Leng,X., Zhang,Q., Zhu,Y.-Z., Zhou,R., Liu,Y., Mei,C., Zhang,D., Liu,S., Chen,S., *et al.* (2024) IRF3 activates RB to authorize cGAS-STING-induced senescence and mitigate liver fibrosis. *Sci Adv*, **10**, eadj2102.

62. Victorelli,S., Salmonowicz,H., Chapman,J., Martini,H., Vizioli,M.G., Riley,J.S., Cloix,C., Hall-Younger,E., Machado Espindola-Netto,J., Jurk,D., *et al.* (2023) Apoptotic stress causes mtDNA release during senescence and drives the SASP. *Nature*, **622**, 627–636.

63. Chen,Y.-A., Shen,Y.-L., Hsia,H.-Y., Tiang,Y.-P., Sung,T.-L. and Chen,L.-Y. (2017) Extrachromosomal telomere repeat DNA is linked to ALT development via cGAS-STING DNA sensing pathway. *Nat Struct Mol Biol*, **24**, 1124–1131.

64. Lu,Y., Zhao,M., Chen,L., Wang,Y., Liu,T. and Liu,H. (2024) cGAS: action in the nucleus. *Front Immunol*, **15**, 1380517.

65. Huang,W., Hickson,L.J., Eirin,A., Kirkland,J.L. and Lerman,L.O. (2022) Cellular senescence: the good, the bad and the unknown. *Nat Rev Nephrol*, **18**, 611–627.

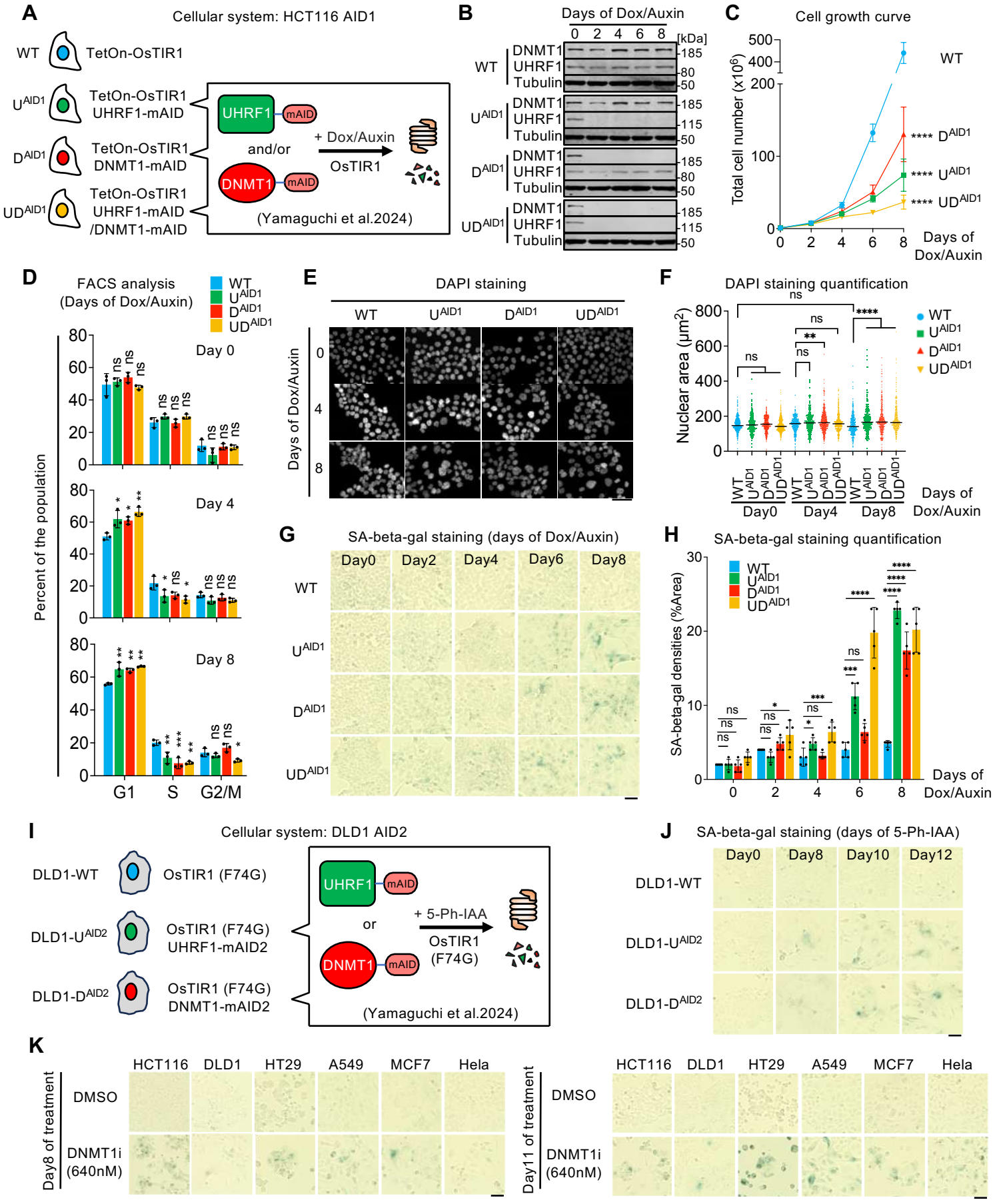

Figure 1. Prolonged UHRF1 or DNMT1 depletion triggers senescence in cancer cells.
(A) The auxin degron system in HCT116 cells conditionally expressing OsTIR1. (B) Western blot validating the degradation of UHRF1 and/or DNMT1 upon Dox/auxin treatment. (C) Cell growth measurements, N = 3 biological replicates. (D) Cell cycle analysis by FACS with BrdU and PI staining. N = 3 biological replicates. (E) Representative images of DAPI staining the indicated lines. (F) Nuclear area determination by DAPI staining. (G) Representative images of SA-β-gal staining after Dox/Auxin treatment. (H) Quantification of SA-β-gal densities. N = 5 fields of view. (I) The auxin degron system in DLD1 cells constitutively expressing OsTIR1 (F74G). (J) Representative images of SA-β-gal staining after Dox/Auxin treatment. (K) Representative images of SA-β-gal staining after treatment of the indicated cells with DMSO or DNMT1 inhibitor GSK-3685032 (640nM) for the indicated duration. Data of (C), (D), and (H) are presented as mean ± SD. Data of (H) are presented as medium. All scale bars are 50μm. * $p < 0.05$, ** $p < 0.01$, *** $p < 0.001$, **** $p < 0.0001$, ns: non-significant (one-way ANOVA or Kruskal-Wallis test with Dunn's multiple comparisons test).

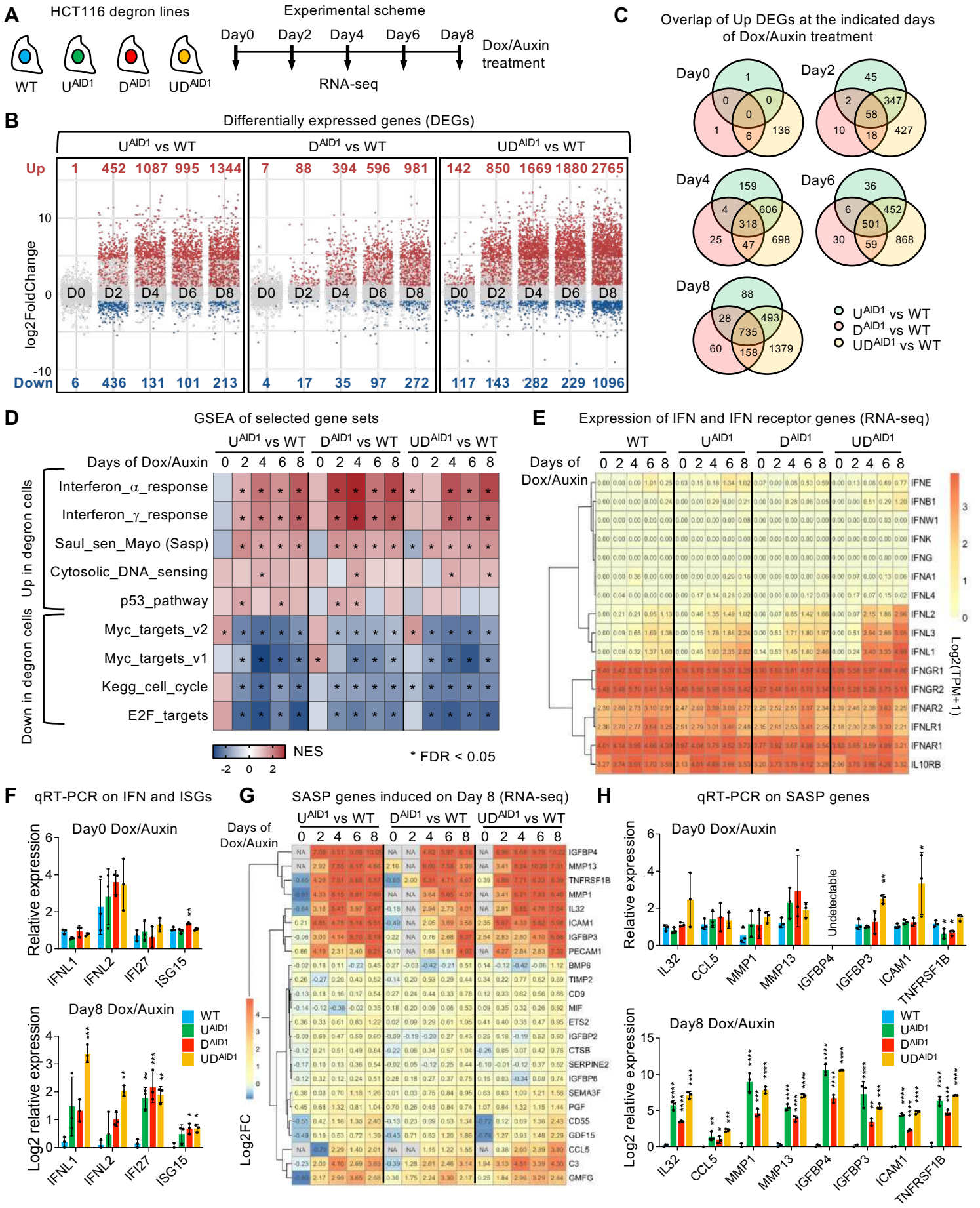

Figure 2. DNA demethylation-induced senescence exhibits an interferon response and a SASP signature.
(A) Experimental scheme. (B) Number of Differentially expressed genes (DEGs). Up-regulated genes (red): adjusted p value < 0.05 and log2 FoldChange > 1. Down-regulated genes (blue): adjusted p value < 0.05 and log2 FoldChange < -1. Light grey dots: no significant change. (C) Venn diagram of significantly up-regulated DEGs at the indicated days. (D) Gene set enrichment analysis (GSEA) of selected gene sets from the Molecular Signatures Database (MSigDB). The heatmap represents the normalized enrichment score (NES) in each comparison at indicated days. Significantly enriched gene sets are shown in red; significantly depleted gene sets are displayed in blue. Conditions with an asterisk are significant with a false discovery rate (FDR) < 0.05. (E) mRNA abundance for interferon (IFN) and IFN receptor genes (using log2-transformed transcripts per million (TPM)). Rows are grouped by hierarchical clustering. (F) qRT-PCR on IFN and IFN-stimulated genes (ISGs). N = 3 biological replicates. (G) Changes in mRNA abundance of SASP genes (log2 FoldChange). (H) qRT-PCR on selected SASP genes. N = 3 biological replicates. Unless otherwise specified, * p < 0.05, ** p < 0.01, *** p < 0.001, **** p < 0.0001, ns: non-significant (one-way ANOVA or Kruskal-Wallis test with Dunn's multiple comparisons test).

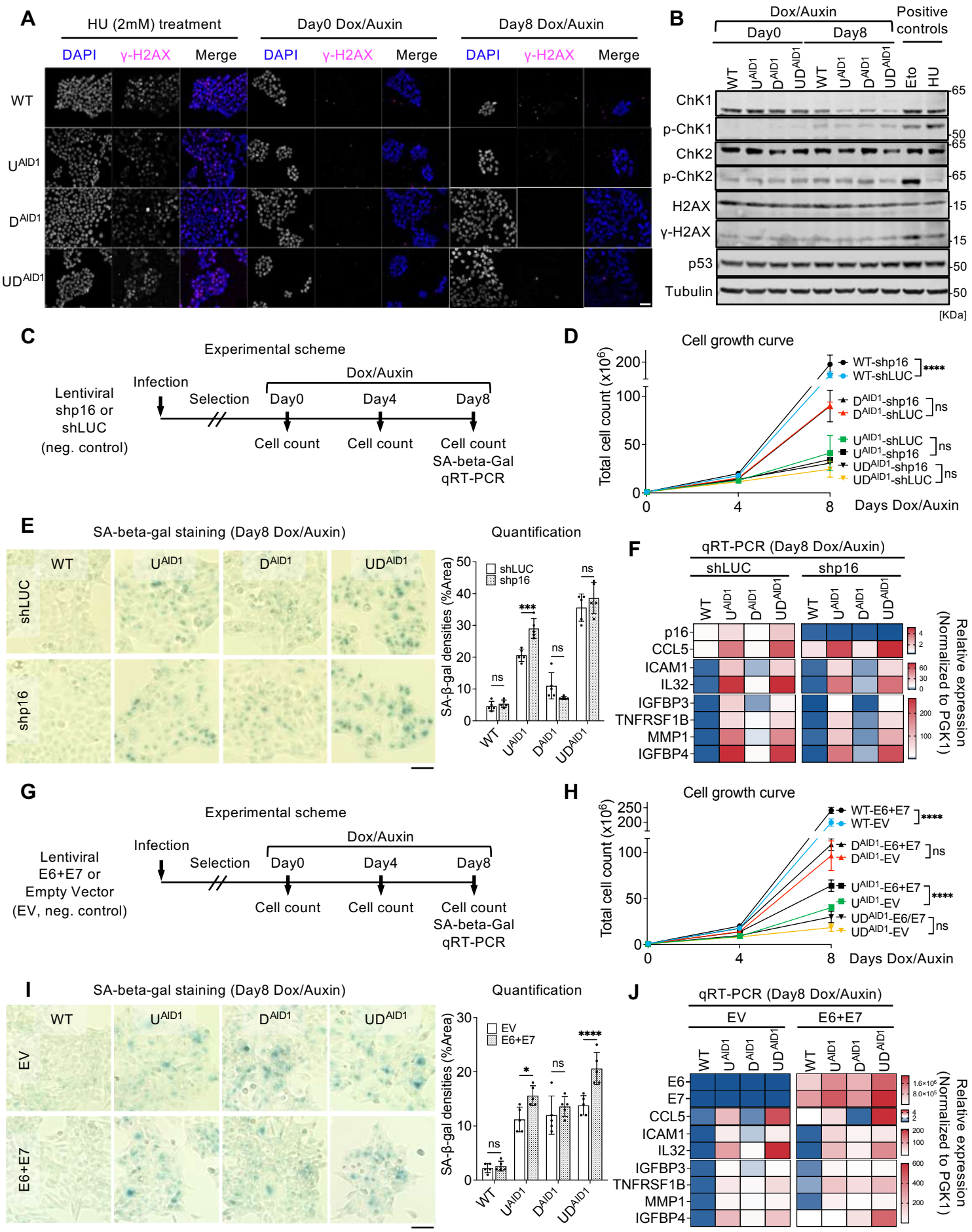

Figure 3. DNA demethylation-induced senescence is independent of p53 and p16/Rb.
(A) γ-H2AX Immunofluorescence in HCT116 lines upon hydroxyurea treatment (HU, 2mM, 4 hours) or upon Dox/Auxin treatment (B) Immunoblots for CHK1, phosphorylated CHK1, CHK2, phosphorylated Chk2, total H2AX, γ-H2AX and p53 in HCT116 lines upon Dox/Auxin treatment. WT HCT116 treated with Etoposide (Eto, 10μM 4 hours) or hydroxyurea (HU, 2mM, 4 hours) used as positive controls. (C) Experimental scheme of p16 depletion and assessment. (D) Total cell numbers at the indicated days of Dox/Auxin. N = 3 technical replicates. (E) SA-beta-gal staining and quantification of indicated lines. N = 5 fields of view. (F) qRT-PCR results of p16 (CDKN2A) and selected SASP genes in indicated conditions. (G) Experimental scheme of E6+E7 expression and assessment. (H) Total cell numbers at the indicated days of Dox/Auxin. N = 3 technical replicates. (I) SA-beta-gal staining and quantification of indicated lines. N = 5 fields of view. (J) qRT-PCR results of E6, E7 and selected SASP genes in indicated conditions. Data of (D, E, H and I) are presented as mean ± SD. Data of (F and J) are presented as mean. All scale bars are 50μm. * $p < 0.05$, *** $p < 0.001$, **** $p < 0.0001$, ns: non-significant (two-way ANOVA with Tukey's multiple comparisons test).

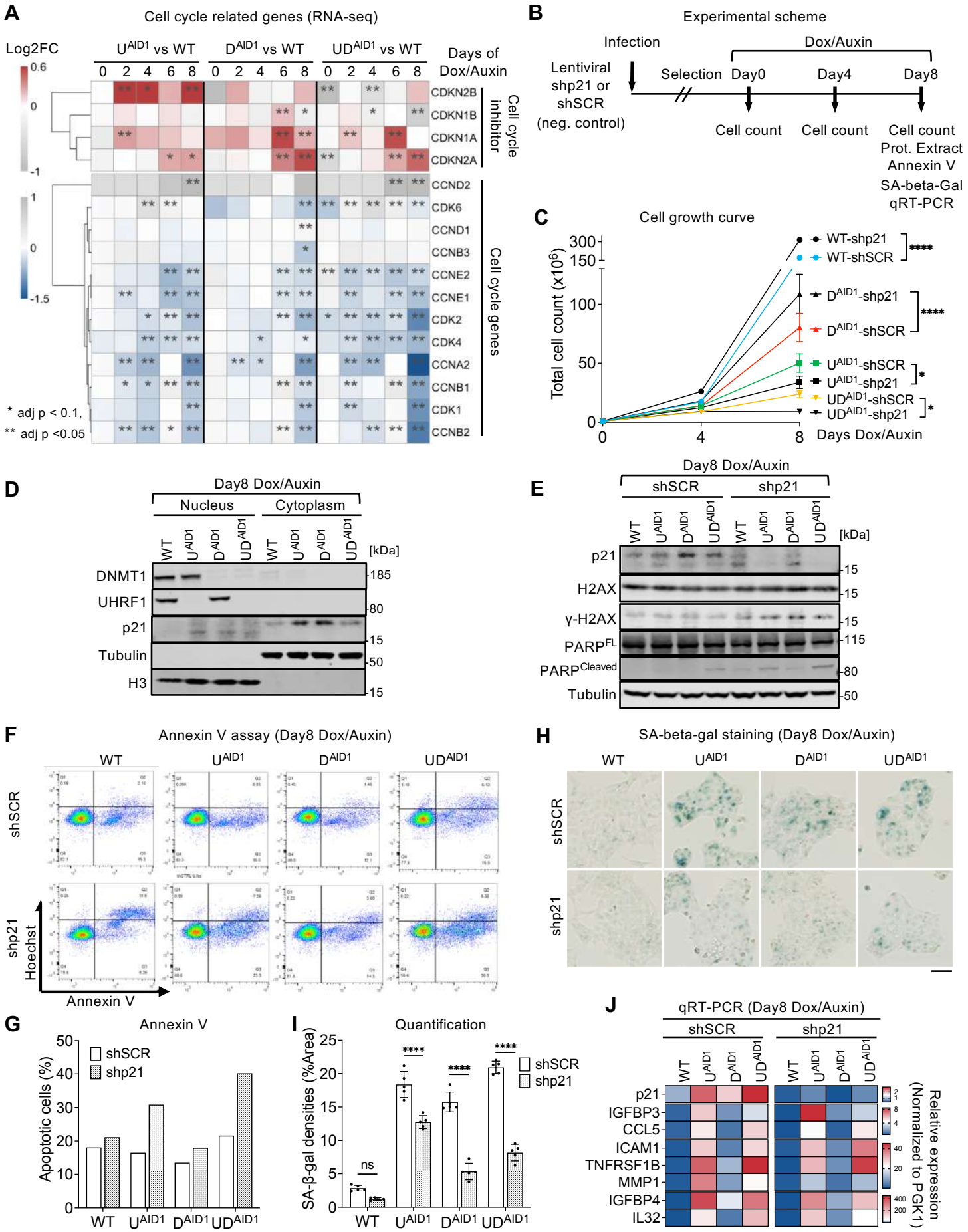

Figure 4. Cytosolic p21 upregulation contributes to anti-apoptosis during senescence.
(A) Changes in mRNA abundance of cell cycle related genes (log2 FoldChange). (B) Experimental scheme of p21 depletion and assessment. (C) Total cell numbers at the indicated days of Dox/Auxin. N = 3 technical replicates. (D) Immunoblots for DNMT1, UHRF1, p21 in the nuclear and cytoplasmic fractions of indicated lines. (E) Immunoblots of p21, H2AX, γ-H2AX, full length PARP and cleaved PARP in indicated lines. (F) Representative results of Annexin V/Hoechst 33342 double staining in indicated lines. (G) Percentages of apoptotic cells (Annexin V positive). (H) SA-beta-gal staining and quantification (I) of indicated lines. N = 5 fields of view. Scale bar: 50μm (J) qRT-PCR results of p21 and selected SASP genes in indicated conditions. Data of (C and I) are presented as mean ± SD. data of (J) is presented as mean. Unless otherwise specified, * p < 0.05, **** p < 0.0001, ns: non-significant (two-way ANOVA with Tukey's or Sidak's multiple comparisons test).

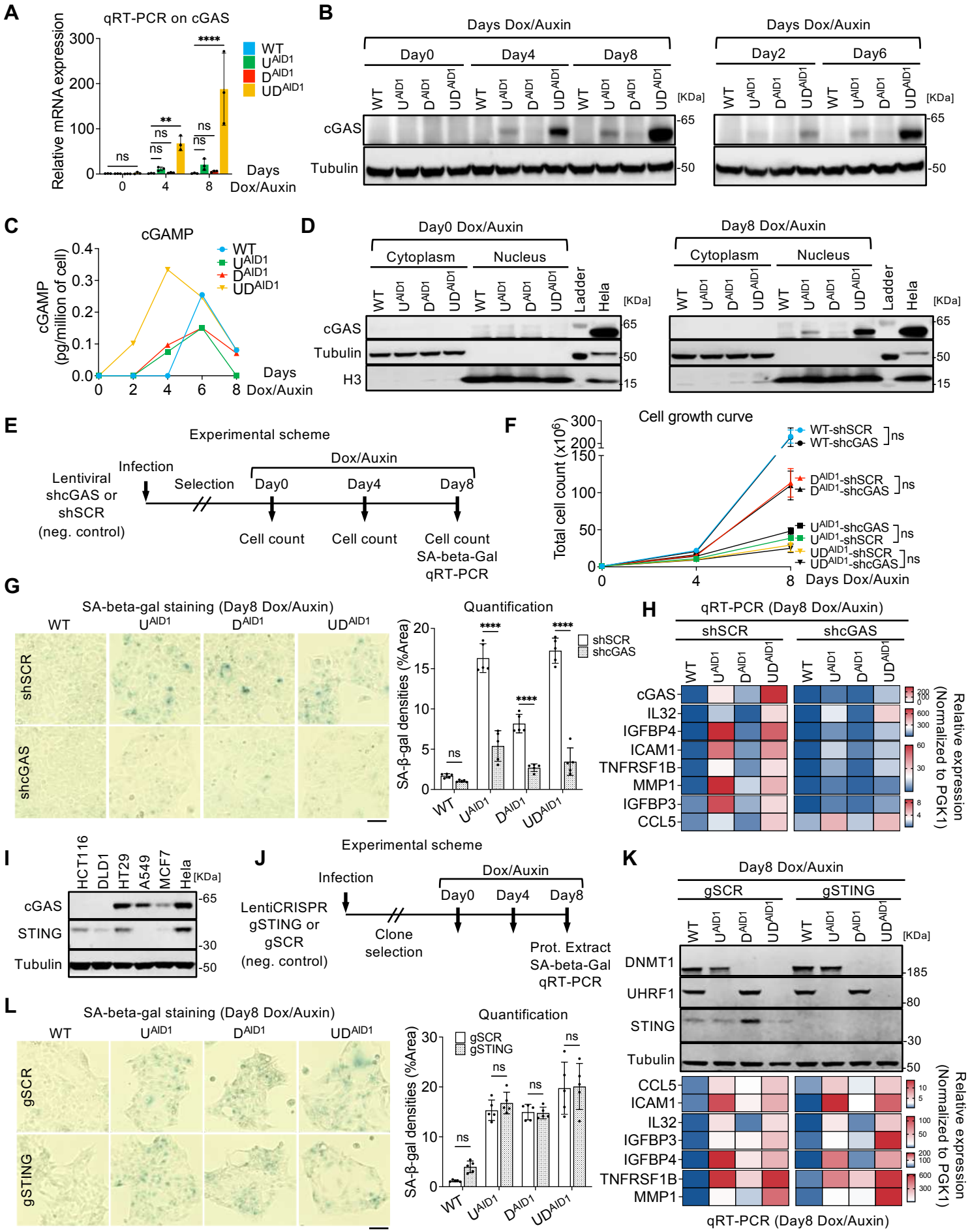

Figure 5. cGAS contributes to SA-beta-gal activity and SASP factor expression, which is independent of STING.
(A) qRT-PCR of cGAS gene expression in HCT116 lines at indicated time points. N = 3 biological replicates. (B) Western blot of cGAS protein in HCT116 lines upon Dox/Auxin treatment at Day0, Day4, Day8 (left panel), Day2 and Day6 (right panel). (C) ELISA detection of cGAMP in HCT116 lines at indicated days. (D) Western blot of cGAS in cytoplasmic and nuclear fractions of HCT116 lines at Day0 (left panel) and Day8 (right panel). (E) Experimental scheme of cGAS knockdown and assessment. (F) Total cell numbers at the indicated days of Dox/Auxin. N = 3 technical replicates. (G) SA-beta-gal staining (left panel) and quantification (right panel) of indicated lines. N = 5 fields of view. (H) qRT-PCR results of cGAS and selected SASP genes in indicated conditions. (I) Western blot of cGAS and STING proteins in different cancer cell lines. (J) Experimental scheme of STING knockout and assessment. (K) Western blot of DNMT1, UHRF1, STING (upper panel) and qRT-PCR results of selected SASP genes (lower panel) in indicated lines. (L) SA-beta-gal staining (left panel) and quantification (right panel) of indicated conditions. N = 5 fields of view. *** $p < 0.001$, **** $p < 0.0001$, ns: non-significant (two-way ANOVA with Tukey's or Sidak's multiple comparisons test).

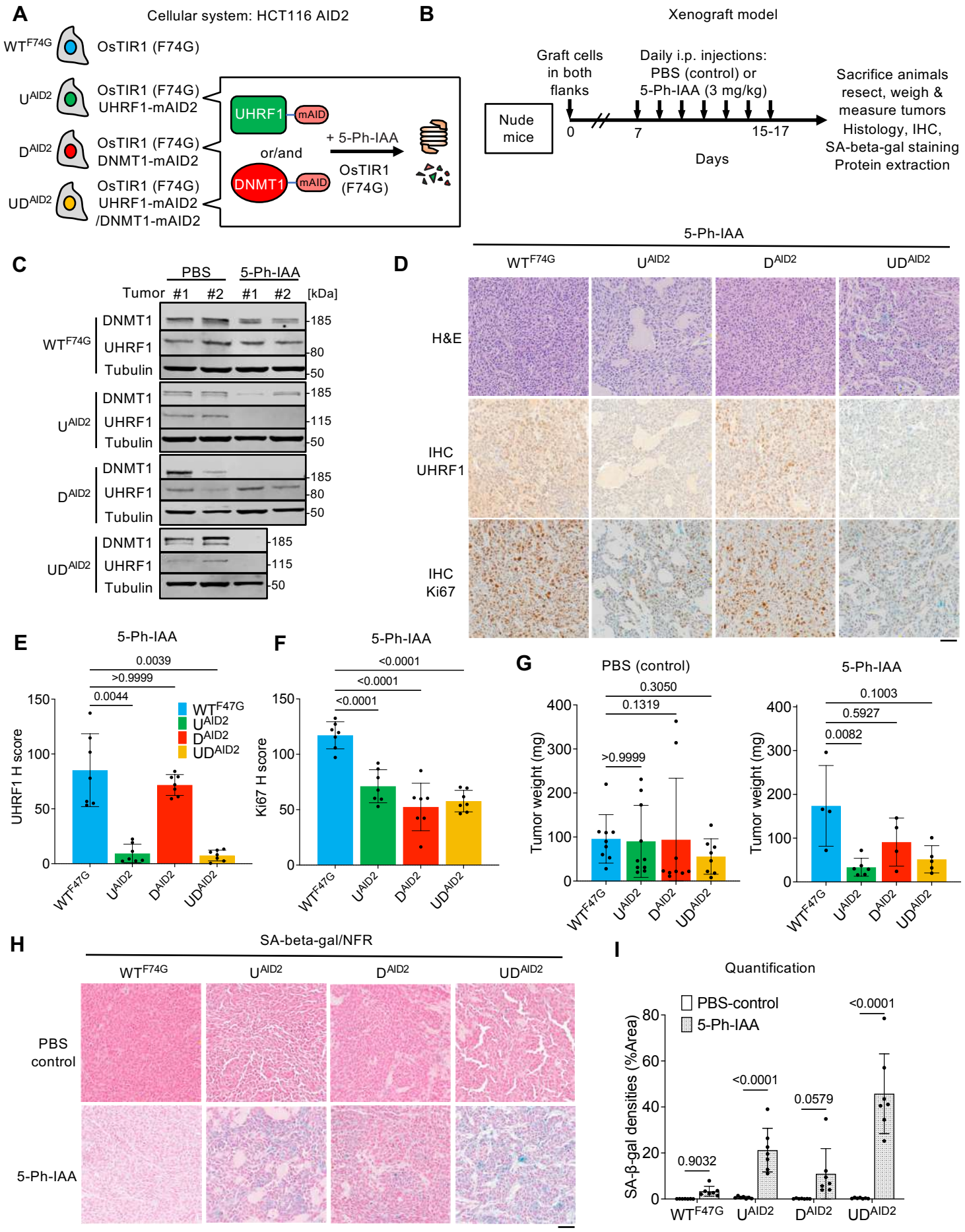

Figure 6. DNA demethylation also triggers senescence in vivo.
(A) The auxin degron system in HCT116 cells constitutively expressing OsTIR1 (F74G). (B) The experimental scheme of xenograft model and assessment. (C) Western blot validating the degradation of UHRF1 and/or DNMT1 upon 5-Ph-IAA (3 mg/kg) treatment in xenograft model. (D) Hematoxylin and eosin (H&E) and immunohistochemistry (IHC) staining of UHRF1 and Ki67 in indicated conditions. (E) Quantification of UHRF1 using H score. N = 7 fields of view at 400x original magnification. (F) Quantification of Ki67 using H score. N = 7 fields of view at 400x original magnification. (G) Tumor weight assessment of indicated conditions. N = 5 mice (control) or 3 mice (5-Ph-IAA). (H) Representative images of SA-beta-gal staining in indicated conditions. Nuclear Fast Red (NFR) was used for counterstaining. (I) Quantification of SA-beta-gal intensities. N = 7 fields of view at 300x original magnification. All data are presented as mean ± SD. All scale bars are 50μm.